# 6

# Electrochemical Passive Properties of $Al_xCoCrFeNi$ (x = 0, 0.25, 0.50, 1.00) High-Entropy Alloys in Sulfuric Acids

Swe-Kai Chen
*Center for Nanotechnology, Materials Science, and Microsystems (CNMM), National Tsing Hua University, Hsinchu, Taiwan*

## 1. Introduction

### 1.1 Pseudo-unitary lattice with a characteristic parameter as a description of multi-principal alloys – The high-entropy alloys (HEAs)

In the summer of 1995, J.W. Yeh and the author (SKC) started the study of multi-principal-element alloys which was called, then, alloys with high randomness and now the high-entropy alloys (HEAs). SKC checked the first 10 equal-molar alloys, which was designed by Yeh that contained from 6 to 9 elements in the alloys out of one of Al, Cu, and Mo, together with Ti, V, Fe, Ni, Zr, Co, Cr, Pd, and B, with a home-made vacuum-arc remelter, and the author observed that the alloy series containing Mo can be made most easily, while the ones containing 3 at% B are the ones most difficult in melting, and 6 out of 10 can be formed in the water-cooled copper mold of the remelter, i.e., the existence of the HEAs was demonstrated by experiments. The alloys were aimed at that time to design as another kind of bulk glass alloys, and based on the high configurational entropy of R ln(n), n between 5 and 13, similar to the mixing of different gases [1]. No conclusions were drawn with XRD patterns of these alloys that were found two years later to be composed with peaks from a single simple lattice cell like FCC A1 or BCC A2, although some evidence of existence of amorphous phase was observed from TEM diffraction patterns and high resolution images [2,3]. The simple crystalline phases instead of amorphous ones were continuously found in alloys like in AlCoCrCuFeNi during research of HEAs in these 10 to 20 years, and identified with a so-called extended FCC or BCC unit cell that SKC called it a pseudo-unitary lattice in 2010 [4].

As multiple principal element alloys, high-entropy alloys (HEAs) comprise at least five elements whose concentration for each one ranges between 5 at % and 35 at % [5]. Attributes of forming a simple solid solution and nano-particle precipitation, as well as achieving a high hardness and strength, and excellent high-temperature oxidation resistance make HEAs highly promising for application and research and development of these alloys [6-9]. Properties of $Al_xCoCrFeNi$ ($0 \le x \le 1$) HEAs vary significantly with x [10]. For instance, the alloy structure changes from FCC to BCC for increased Al content x. Besides, the coefficient of thermal expansion decreases with x. Both properties are closely related to the bond strength of alloys. Moreover, electrical resistivity of $Al_xCoCrFeNi$ alloys is large, i.e., approximately up to 200 $\mu\Omega$ cm [11].

### 1.2 Corrosion resistance for HEAs and conventional alloys

Corrosion properties of $AlCoCrCu_{0.5}FeNiSi$ [12,13], $Al_xCrFe_{1.5}MnNi_{0.5}$ [14,15], and $Al_{0.5}CoCrCuFeNiB_x$ [16] HEAs have been extensively studied in recent years. Among these HEAs, $AlCoCrCu_{0.5}FeNiSi$ alloy (HEA 1) displays, at room temperature, a better general corrosion resistance than SS 304 in 1 N $H_2SO_4$; however, it exhibits a worse pitting corrosion resistance than SS 304 in 1 N $H_2SO_4$ and in 1 M NaCl, respectively. The general corrosion resistance of each of HEA 1 and SS 304 decreases when exceeding room temperature. The effect of temperature on corrosion resistance of HEA1 is less severe in 1 M NaCl than in 1 N $H_2SO_4$ [13]. $Al_xCrFe_{1.5}MnNi_{0.5}$ alloys (HEA 2) reveal that in each of the 0.5 M $H_2SO_4$ and 1 M NaCl solutions, corrosion resistance increases with a decreasing x; in addition, the susceptibility to general and pitting corrosion of HEA 2 increases with an increasing x [14]. $Al_xCrFe_{1.5}MnNi_{0.5}$ alloys (called hereinafter as HEA 2a and 2b for x = 0 and 0.3, respectively) in 0.1 M HCl exhibit different corrosion behaviours for different x values. Although HEA 2a is susceptible to localized corrosion, HEA 2b has a stable passive film on the surface. In 0.1 M HCl, anodized treatment of HEA 2a and 2b alloys in 15 % $H_2SO_4$ gives higher corrosion resistance than the untreated [15]. In deaerated 1 N $H_2SO_4$, $Al_{0.5}CoCrCuFeNiB_x$ alloys are more resistant to general corrosion than SS 304, and are not susceptible to localized corrosion. Additionally, the corrosion resistance of $Al_{0.5}CoCrCuFeNiB_{0.6}$ alloy is inferior to $Al_{0.5}CoCrCuFeNi$ alloy [16]. Above HEAs show an extremely close compositional dependence of corrosion behaviour in various solutions.

### 1.3 Aim of this study

Although many interesting topics have been explored for $Al_xCoCrFeNi$ alloys [10,11], investigation on their corrosion property is still lacking. Therefore, this study elucidates how Al affects their corrosion behaviour. The electrochemical properties of the alloys in sulfuric acids are investigated using the potentiodynamic polarization curve and a weight loss measurement method. Additionally, these alloys are compared with SS 304, especially with respect to the effect of temperature. Moreover, based on use of electrochemical impedance spectroscopy (EIS), the effect of Al on corrosion behaviour is analyzed. Furthermore, the relationship of stability of oxide film with Al content is examined by varying the chloride concentration in a sulfuric solution. Additionally, this study, which extends [17], also attempts to investigate the mechanism of the passive layers influenced by Al content x at various temperatures in detail.

## 2. Experimental details

### 2.1 Test materials and conditions for electrochemical and weight loss tests

#### 2.1.1 Test specimens for electrochemical tests and weight loss measurements

As-cast $Al_xCoCrFeNi$ alloys were prepared according to molar ratios of x = 0, 0.25, 0.50, and 1.00 (called C-0, C-0.25, C-0.50, and C-1.00, respectively) in a vacuum arc remelter. Table 1 lists the composition of the alloys. Test specimens were cut in 0.8 cm x 0.8 cm x 0.3 cm and cold-mounted in epoxy with the outside surface from a surface of 0.8 cm x 0.8 cm of specimens. The specimens were subsequently ground and polished with grit #1000 silicon carbide paper, rinsed and dried in preparation for electrochemical tests and weight loss measurements. During determination of the weight loss, six sets of samples were dipped in

sulfuric acid for 1, 3, 5, 8, 11, and 15 days, respectively. All tests, except the weight loss test, were performed at least three times to confirm the data reproducibility. Finally, weight loss tests were performed twice and the reproducibility was given in an error bar.

| Alloys | Al | Co | Cr | Fe | Ni |
|---|---|---|---|---|---|
| C-0 | 0 | 27.12 | 23.74 | 23.99 | 25.14 |
| C-0.25 | 3.05 | 25.14 | 22.48 | 24.15 | 25.18 |
| C-0.50 | 5.59 | 25.25 | 22.13 | 22.80 | 24.22 |
| C-1.00 | 10.02 | 23.84 | 21.11 | 21.99 | 23.03 |
| SS 304 | 0 | 0 | 19.40 | 72.68 | 7.92 |

Table 1. Composition (wt %) for alloys C-x and SS 304.

#### 2.1.2 Test solutions and temperatures

The base solution for all tests was 0.5 M of sulfuric acid. Test temperatures were ambient temperature (~25°C). Test solutions bearing chloride ions were with 0.25, 0.50, and 1.00 M sodium chloride in the base solution. To avoid the dissolved oxygen (aeration) affecting the test solutions, deaeration was simultaneously made by a nitrogen gas flow of 120 ml/min in the test solution. The effect of temperature on polarization was examined under thermostatic control at an interval of 15°C in the temperature range of 20°C - 65°C.

### 2.2 Potentiodynamic polarization curve measurements and electrochemical impedance spectroscopy (EIS)

A three-electrode cell was used for the electrochemical test. The reference electrode was a commercial Ag/AgCl electrode saturated in 3 M KCl electrode (−0.205 $V_{SHE}$ or –0.205 V to standard hydrogen electrode). The auxiliary electrode was made of Pt, and the working electrode was the specimen. Potentiostat was CH Instrument Model-600A. The specimen was cathodically polarized at a potential of −0.4 $V_{SHE}$ for 300 s before the test for the purpose of removing surface oxides. The quasi-steady-state time for an open circuit was 900 s. Scan speed was 1 mV/s for scan potential ranging from −0.6 $V_{SHE}$ to 1.4 $V_{SHE}$. For EIS, the working potential was that of open circuit at 900 s from the start of immersion with scan amplitude 10 mV and a frequency ranging from 100 kHz to 10 mHz.

### 2.3 Immersion tests and ICP-AES and XPS analyses

Samples were dipped in sulfuric acid for 15 d to determine the weight-loss rate. Auger electron spectroscopy (AES) and X-ray photoelectron spectroscopy (XPS) analysis were performed with samples after a 0.8 $V_{SHE}$ pretreatment plus a 1-h immersion. Inductively coupled plasma atomic emission spectroscopy (ICP-AES) was performed on the electrolyte after an 8-d immersion of the samples. The effect of temperature on polarization was examined under thermostatic control at an interval of 15°C in the temperature range of 20°C–65°C.

### 2.4 Scanning electron microscopy (SEM) metallographic examination and energy dispersed X-ray spectroscopy (EDS) analysis

Samples were fine polished, up to 0.05 μm $Al_2O_3$ powder and, then, examined with SEM (JEOL JSM-840A) equipped with an Oxford EDS for topography and elemental

compositions. Finally, samples were examined before and after 3 days immersion of 0.5 M $H_2SO_4$.

## 3. Results and discussion

### 3.1 Potentiodynamic polarization curve and weight loss at 25 °C

Fig. 1 shows the anodic dissolution behaviour of alloys in 0.5 M $H_2SO_4$, while Table 2 summarizes relevant data. This figure reveals a well-defined passive region of 0 $V_{SHE}$ to 1.2 $V_{SHE}$ in all curves. All curves, except for the one at x = 0.25 (C-0.25), show a secondary passive region at 0.15 $V_{SHE}$. This passivation is attributed mainly to the further oxidation or hydroxidation of the passive oxide film, thus altering the valence of Cr [18,19]. Fig. 1 also indicates that the secondary passive regions of C-0.50 and C-1.00 are more prominent than those of C-0 and C-0.25. This observation is due to the selective dissolution in the duplex FCC-BCC structure for C-0.50 and in the BCC-ordered BCC structure for C-1.00, as compared with C-0 and C-0.25 which are single FCC phase. In the active-passive transition region, different compositions at different secondary passivation potentials reveal different dissolution rates owing to a selective dissolution. This observation resembles that observed in duplex phase stainless steel [20,21].

| Alloys C-x & SS304 | $E_{corr}$ ($V_{SHE}$) | $I_{corr}$ ($\mu A/cm^2$) | $E_{pp}$ ($V_{SHE}$) | $I_{crit}$ ($\mu A/cm^2$) | $I_{pass}$ ($\mu A/cm^2$) |
|---|---|---|---|---|---|
| C-0 | -0.081 | 15.8 | 0.002 | 42.8 | 4.5 |
| C-0.25 | -0.095 | 16.7 | 0.008 | 87.4 | 7.1 |
| C-0.50 | -0.084 | 13.4 | 0.017 | 117.2 | 6.4 |
| C-1.00 | -0.094 | 13.1 | 0.010 | 198.0 | 13.9 |
| SS 304 | -0.185 | 45.3 | -0.071 | 603.0 | 19.1 |

Table 2. Potentiodynamic polarization curve diagram parameters of alloys C-x and SS 304 at 25°C.

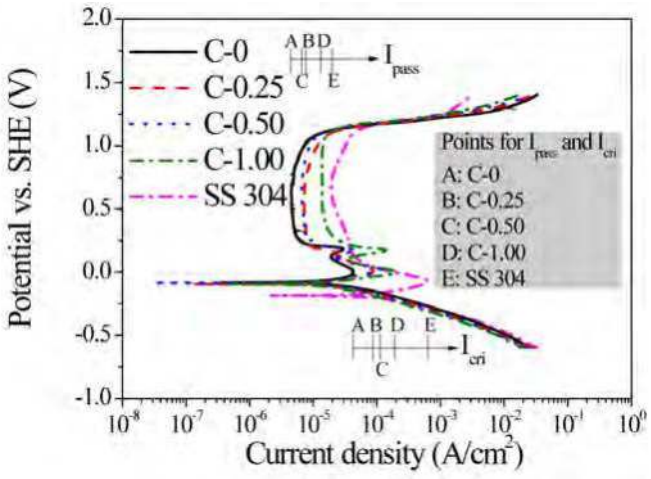


Fig. 1. Potentiodynamic polarization curve diagrams for alloys C-x and SS 304 at 25°C.

Table 2 reveals that the corrosion potential ($E_{corr}$) and the corrosion current density ($I_{corr}$) for all of the alloys differ only slightly, and no obvious trends occur for $E_{corr}$ and $I_{corr}$ vs. x variation. The above phenomenon can be attributed to the spontaneous passivation of pure Al in $H_2SO_4$ [22]. Al metal spontaneously passivates in $H_2SO_4$, explaining why its corrosion potential is ready in the passive region, i.e., this passivation explains why the polarization curve of Al does not display an apparent active-passive transition region. However, elements such as Cr and Fe exhibit a large critical current density ($I_{cri}$) for passivation, explaining why Cr and Fe dissolve more than Al before the alloy reaches its passive state. Thus, the variation of Al affects the active region of the polarization curves slightly. Furthermore, in $H_2SO_4$, all Al, Co, Cr, Fe, and Ni metals show passivity. Among them, Al has a relatively high passive current density ($I_{pass}$) [22,23] because only Al oxide can easily form a porous film on the metal surface [24]. Therefore, protection by oxide layer on the alloys with higher Al content is inferior to that with lower Al content. Fig. 1 thus reveals that $I_{pass}$ increases with x.

The results of potentiodynamic polarization were compared via performing 15-day-dipping and weight loss experiments. In the 15-day-dipping and weight loss experiments, the corrosion rates for C-0.50 and C-1.00 were markedly higher than those of C-0 and C-0.25 (Fig. 2). This observation differs substantially from the values of $I_{corr}$ obtained from polarization experiment (Fig. 1), in which the two groups only differ slightly, despite the fact that the trend is the same. A previous study found a similar deviation in corrosion current densities obtained from weight loss test and potentiodynamic polarization method [25].

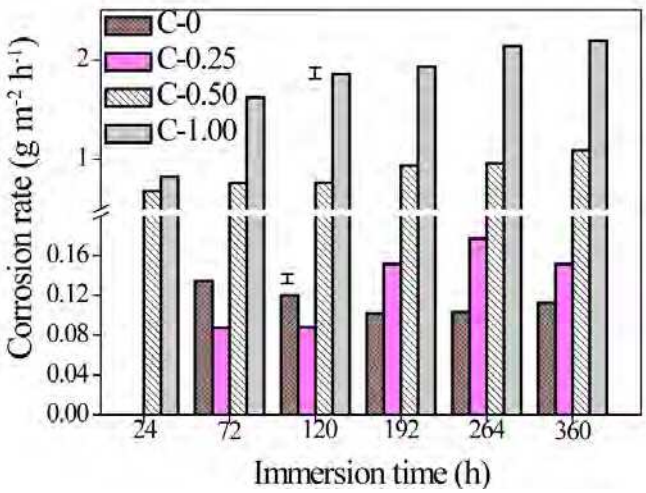


Fig. 2. Diagram showing change in corrosion rate (g $m^{-2}$ $h^{-1}$) in the 15-day-dipping and weight loss measurement for alloys C-x.

Fig. 1 shows potentiodynamic polarization diagrams for the $Al_xCoCrFeNi$ alloys and SS 304. The alloys have better overall general corrosion behaviour, with a larger $E_{corr}$ and smaller $I_{corr}$, $I_{cri}$, and $I_{pass}$ than SS 304.

### 3.2 Effect of temperature on potentiodynamic polarization

Fig. 3 shows polarization diagrams of $Al_xCoCrFeNi$ alloys at various temperatures. A rising temperature decreased the Tafel slopes of anode (Table 3), increased $I_{corr}$, and increased $E_{corr}$ and $E_t$ (the transpassive potential) slightly. The corrosion rate is directly related to $I_{corr}$, according to Arrhenius equation, $I_{corr} = A \exp(-E_a/RT)$ [13,26], where the pre-exponential factor A is generally independent of temperature and is a constant of alloys, where R denotes the gas constant, T denotes temperature, and $E_a$ denotes activation energy for corrosion. In the case of small experimental temperature range, $E_a$ is assumed to be independent of T. Consequently, $E_a$ can be obtained from $\ln(I_{corr})$ vs. 1/T plot. Fig. 4 shows such plots for the alloys and SS 304, indicating that $E_a$ increases with x. This finding suggests that the corrosion rate is more sensitive to temperature for a larger Al content than for a smaller Al content. The $\ln(I_{corr})$ vs. 1/T curves intersect with each other in a range of 23°C – 27°C. Beyond this temperature range, $I_{corr}$ increases with x. The situation is reversed at temperatures lower than 23°C, which is inconsistent with a situation in which $E_a$s for all alloys increase with x from 20°C to 65°C. Hence, $E_a$, i.e., an intrinsic property of metal, and A, i.e., a surface property of metal, are determinative factors of $I_{corr}$. While $E_a$ depends only on x, A depends on both x and temperature (Table 4). Therefore, although $E_a$ increases with x, A also increases with x. Combining the effects of $E_a$ and A explains the different corrosion behaviours of the alloys with an increasing x at temperatures exceeding 27°C and lower than 23°C. Thus, the performance of passive films, when Al is added, at higher temperatures becomes inferior to that without addition of Al. In determining $I_{corr}$, A is more important than $E_a$ at temperatures exceeding 27°C, while $E_a$ is more important than A at temperatures lower than 23°C.

| Alloys | 20 °C | | 35 °C | | 50 °C | | 65 °C | |
|---|---|---|---|---|---|---|---|---|
| C-x | $\beta_a$[a] | $\beta_c$[b] | $\beta_a$ | $\beta_c$ | $\beta_a$ | $\beta_c$ | $\beta_a$ | $\beta_c$ |
| C-0 | 158 | 218 | 128 | 158 | 134 | 162 | 89 | 158 |
| C-0.25 | 158 | 178 | 103 | 167 | 89 | 168 | 92 | 149 |
| C-0.50 | 94 | 158 | 113 | 178 | 138 | 159 | 89 | 198 |
| C-1.00 | 104 | 148 | 93 | 173 | 98 | 242 | 100 | 220 |

[a] Anodic Tafel slope $\beta_a$ in mV/decade, the measured Tafel regions are with 40~50 mV of overvoltage.
[b] Cathodic Tafel slope $\beta_c$ in mV/decade, the measured Tafel regions are with 150~170 mV of overvoltage.

Table 3. Fit data for Tafel slopes of alloys C-x in 20 °C - 65 °C.

| Alloys | A(x, T), A/cm² | | | | $E_a$, kJ/mol |
|---|---|---|---|---|---|
| | 20 °C (293 K) | 35 °C (303 K) | 50 °C (323 K) | 65 °C (338 K) | |
| C-0 | $1.16 \times 10^{-4}$ | $1.16 \times 10^{-4}$ | $1.16 \times 10^{-4}$ | $1.07 \times 10^{-4}$ | 3.96 |
| C-0.25 | $1.90 \times 10^{-4}$ | $2.03 \times 10^{-4}$ | $1.77 \times 10^{-4}$ | $1.90 \times 10^{-4}$ | 5.35 |
| C-0.50 | 7.17 | 5.64 | 3.70 | 8.41 | 31.24 |
| C-1.00 | $1.78 \times 10^{9}$ | $7.46 \times 10^{8}$ | $1.89 \times 10^{9}$ | $1.31 \times 10^{9}$ | 78.61 |
| SS 304 | $1.18 \times 10^{-4}$ | $1.28 \times 10^{-4}$ | $1.70 \times 10^{-4}$ | $2.07 \times 10^{-4}$ | 9.87 |

Table 4. The fits for A(x, T) and $E_a(x)$ in $I_{corr}(x, T) = A(x, T) \exp(-E_a(x)/RT)$.

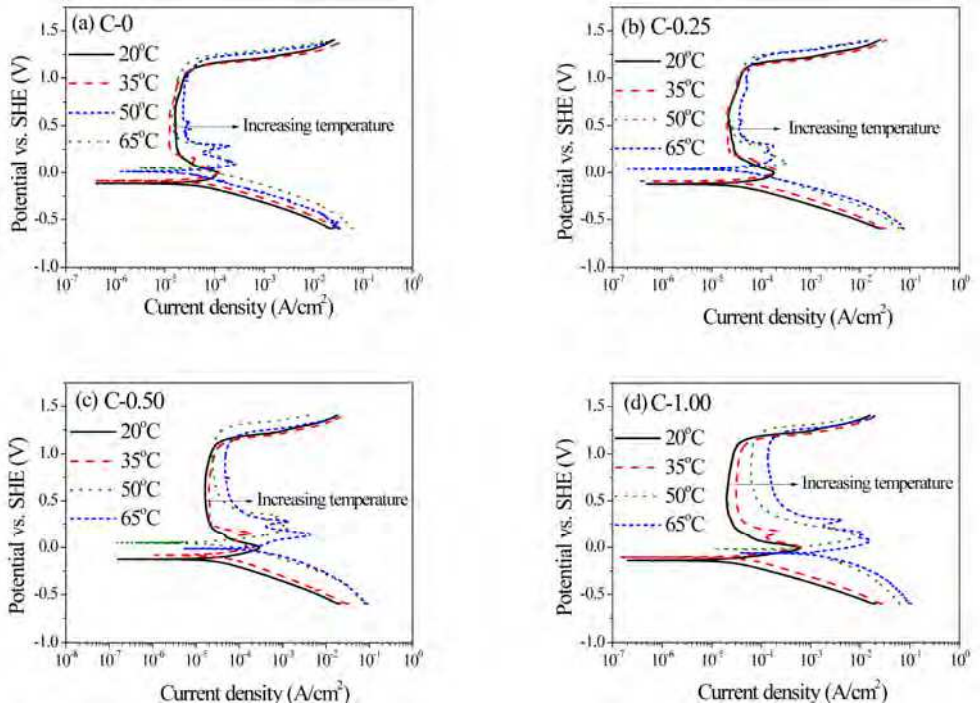


Fig. 3. Potentiodynamic Polarization Curve diagrams for (a) C-0, (b) C-0.25, (c) C-0.50, and (d) C-1.00 at various temperatures.

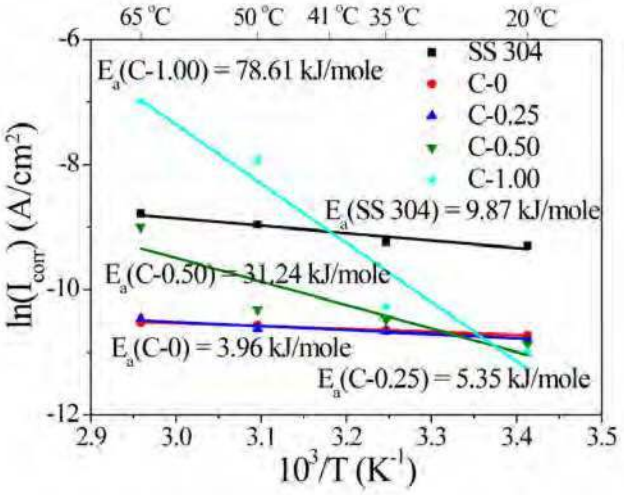


Fig. 4. The Arrhenius plots for alloys C-x and SS 304 at 20°C - 65°C.

### 3.3 EIS test at 25°C

Figs. 5 and 6 summarize the EIS results of alloys in a sulfuric solution and their schematic equivalent circuit diagrams, respectively. Table 3 lists related parameters of the equivalent circuit diagrams, where $R_s$, $R_f$, and $R_{ct}$ denote impedances of the sulfuric solution, oxide layer, and adsorption layer, $Q_f$ and $Q_{ad}$ denote capacitances of constant phase element (CPE) for oxide layer and adsorption layer, respectively. Next, the oxide layer thickness is evaluated by using the Helmholtz model [27] and expressing the layer thickness of the oxide layer, d, as $d = \varepsilon\varepsilon_o S/Q_f$, where $\varepsilon_o$ denotes the permittivity of free space ($8.85 \times 10^{-14}$ F/cm), $\varepsilon$ denotes the dielectric constant of the medium, and S denotes the surface area of the electrode. Assuming that $\varepsilon$ and S for all oxide layers of alloys are the same allows us to compare relative values of d for all samples by $1/Q_f$. Fig. 7 reveals that $1/Q_f$ values are proportional to x, implying that d increases with Al content x. However, according to this figure, the impedance of oxide layer $R_f$ decreases with x and, in Fig. 8, the impedance of the oxide layer is inversely proportional to $I_{pass}$. Restated, a thinner oxide layer implies a larger value of impedance. To explain this phenomenon, besides the thickness of oxide layer, the density of oxide layer is also considered. As mentioned in Section 3.1, Al oxide easily forms a porous film on the metal surface [24]. Therefore, it is easily understood that in addition to causing a thicker oxide layer, Al element promotes the dispersive oxide layer. Combining these two effects obviously reveals that $R_f$ decreases with x.

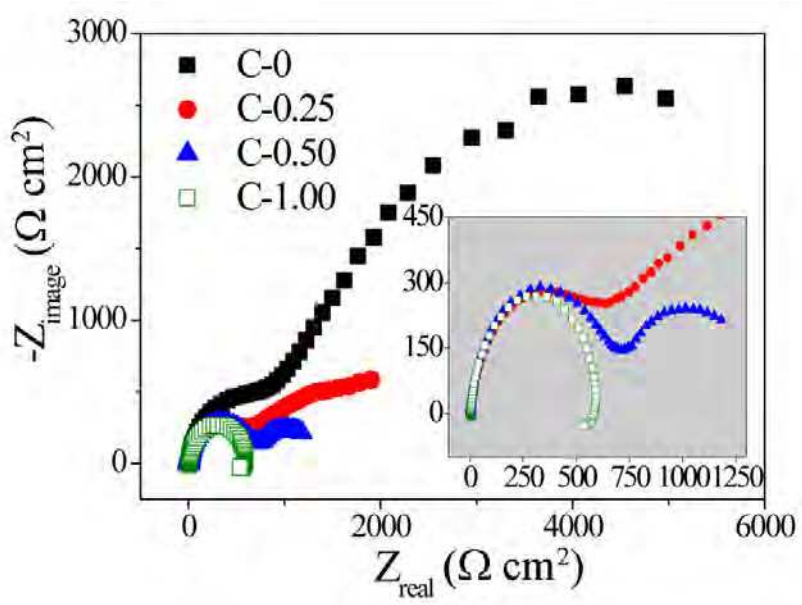


(a)

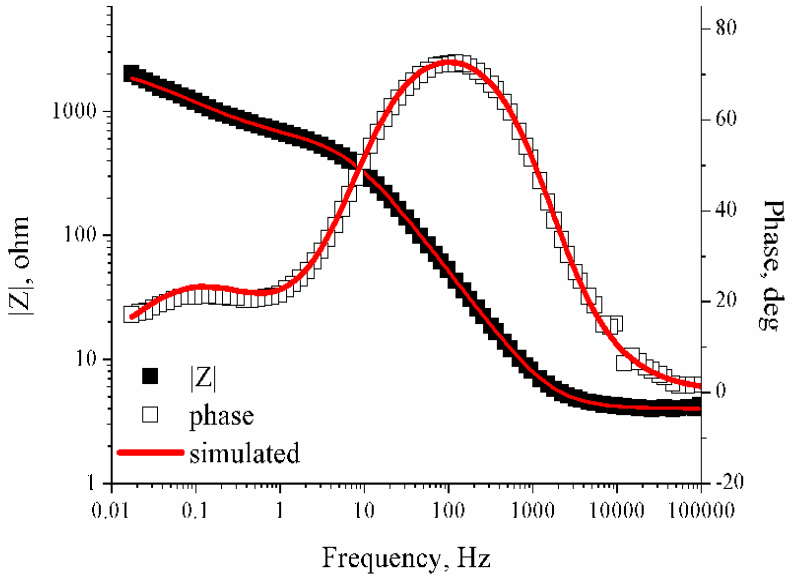


(b)

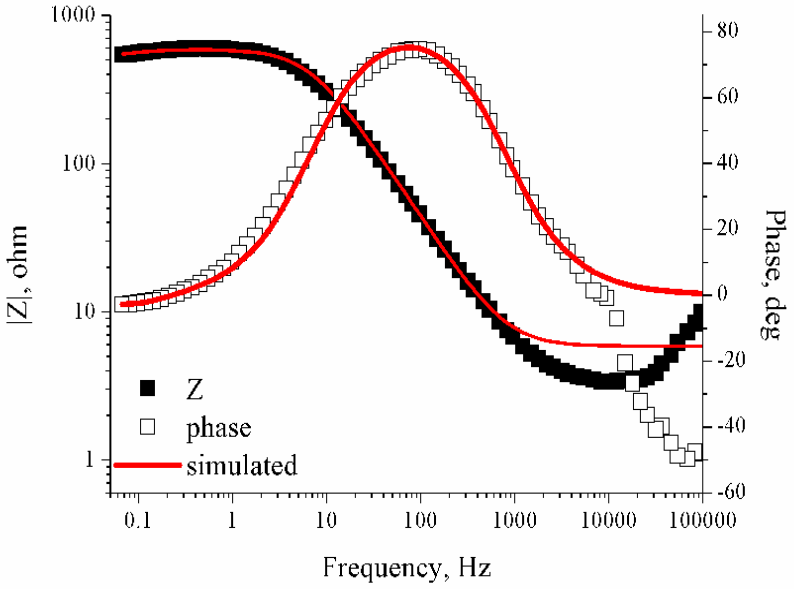


(c)

Fig. 5. (a). The Nyquist plots for alloys C-x at 25°C. (b). The Bode plot for C-0.25. (c). The Bode plot for C-1.00.

According to Fig. 6, only C-1.00 reveals a component of inductance in the equivalent circuit (See Fig. 5(c)). In previous studies [28-31], alloys with Al and Ni readily react with $(OH)^-$ and $(SO_4)^{2-}$ in a sulfuric solution and adsorbed on the surface of the alloys, which increases the amount of the ions in the adsorption layer. Therefore, $Q_{ad}$ increases with x, as listed in Table 5. As x value increases to 1.00, the inductance appears in the equivalent circuit in Fig. 6(b). This effect normally occurs in the case of a severe corrosive condition [32]. Origin of the inductance can generally be influenced by some adsorbed intermediates or can be attributed to a space at the interfaces [33]. In C-1.00, a microstructure with an Al and Ni-rich phase which is seen as a reactive phase from metallograph, not only causes adsorption in these Al and Ni-rich areas in corrosion process, but also decreases the impedance in the low frequency area owing to their continuous dissolution. The fact that $R_{ct}$ decreases with x demonstrates a higher dissolution rate for alloys with a higher Al content.

| Alloys C-x | $R_s$ ($\Omega$ cm$^2$) | $Q_f$ ($\mu$F/cm$^2$) | $n_f$ | $R_f$ ($\Omega$ cm$^2$) | $Q_{ad}$ ($\mu$F/cm$^2$) | $n_{ad}$ | $R_{ct}$ ($\Omega$ cm$^2$) |
|---|---|---|---|---|---|---|---|
| C-0 | 3.271 | 54.57 | 0.9094 | 992.2 | 636.7 | 0.7444 | 7691 |
| C-0.25 | 3.758 | 56.61 | 0.9081 | 610.5 | 1525 | 0.6347 | 1932 |
| C-0.50 | 2.994 | 46.55 | 0.9223 | 642.8 | 3221 | 0.6454 | 819.1 |
| C-1.00 | 3.462 | 47.16 | 0.9614 | 518.1 | $L_{ad}$ | - | 66.81 |

* Lad = 122.4 Henry

Table 5. EIS equivalent circuit parameters for alloys C-x.

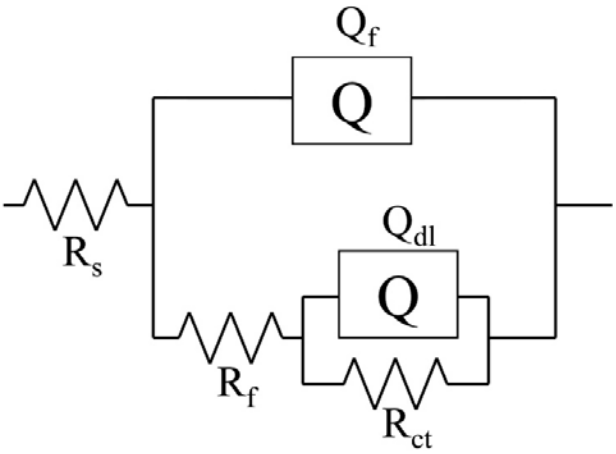


Fig. 6. EIS equivalent circuits for alloys C-0, C-0.25, C-0.50, and C-1.00.

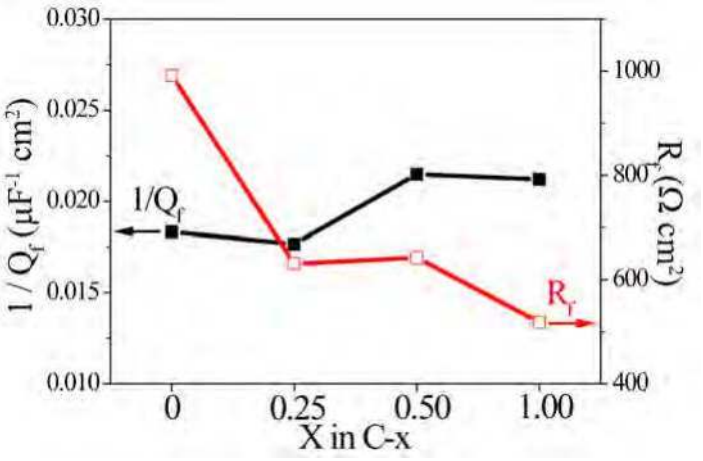


Fig. 7. Impedance and relative thickness ($1/Q_f$) of oxide layer vs. Al content x plots.

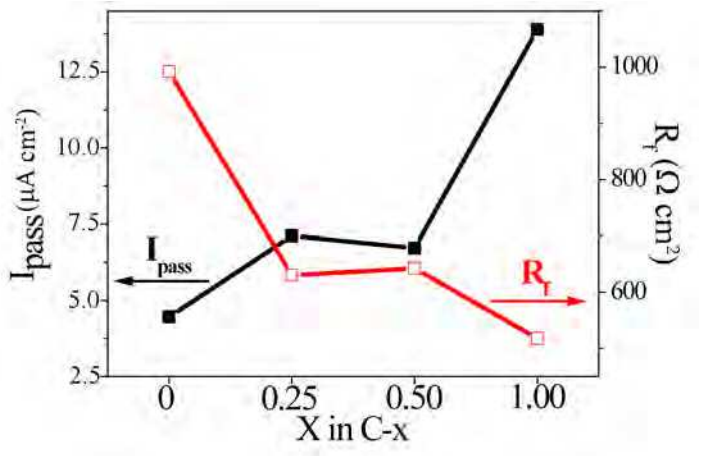


Fig. 8. Impedance and $I_{pass}$ of oxide layer vs. Al content x plots.

### 3.4 Polarization behaviour for alloys in a chloride-containing $H_2SO_4$ solution

Fig. 9 shows potentiodynamic polarization curve diagrams for the alloys in 0.5 M $H_2SO_4$ solution containing various concentrations of chloride ions, as well as in simple 0.5 M $H_2SO_4$ solution as a comparison. According to Fig. 9(a), oscillation occurs in a passive region for C-0 in 0.5 M $H_2SO_4$ containing 0.5 M and 1 M of chloride. This phenomenon has been attributed to the cycling process for small pitting and re-passivation with the duration of several seconds for each cycle [34]. Oscillation in the passive region in potentiodynamic polarization curve is a metastable state [35]. This metastable state generally reflects the difficulty of pitting, i.e., alloy C-0 has good anti-pitting ability, while those containing aluminum (C-0.25, 0.50, and 1.00) with no metastable state show an inferior anti-pitting ability (Figs. 9 (b) to (d)).

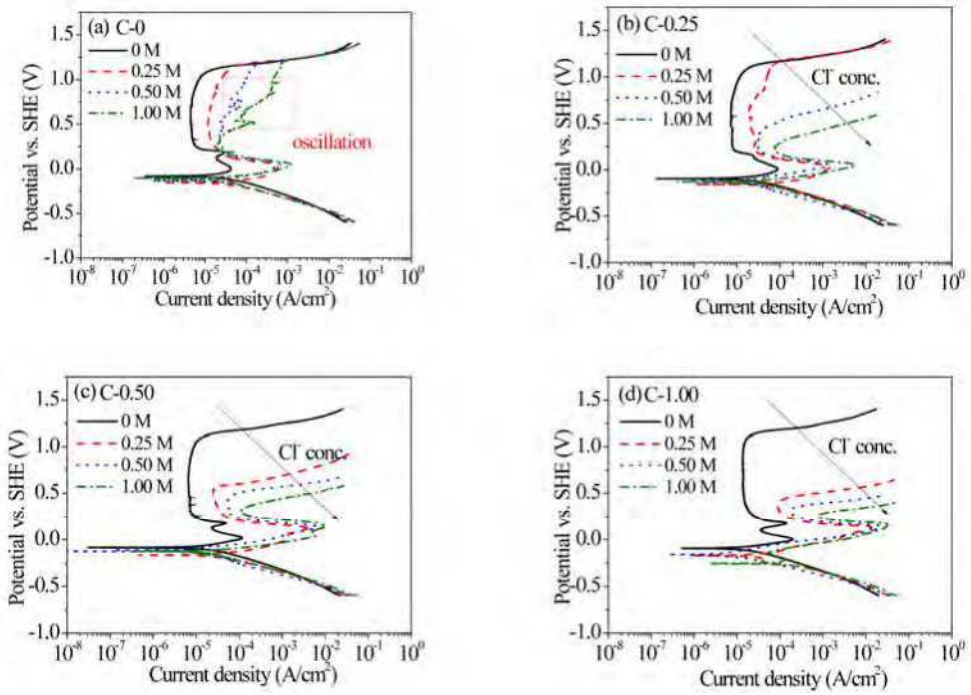


Fig. 9. Potentiodynamic Polarization Curve diagrams for (a) C-0, (b) C-0.25, (c) C-0.50, and (d) C-1.00 at 25 °C in chloride-containing sulfuric acid solution at various $Cl^-$ molarity (M) values.

From an adsorption viewpoint, adsorption competition always prevails on the alloy surface between chloride ions and dissolved oxygen atoms. Notably, no oxide layer forms once chloride ions adsorb on the alloy surface, in which the metal ions readily dissolve. Therefore, the adsorption of chloride ions increases the reacting current density (as indicated by a comparison of Figs. 1 and 9), subsequently increasing the rate of metal dissolution.

Rapid dissolution of alloys in chloride-containing solution is discussed next. When chloride ions are adsorbed on the interface of passive layer and a sulfuric solution, metastable ion complexes gradually form from the anions of a passive layer. These metastable ion complexes enable the anions to dissolve. Once the ion complexes that are on the passive layer/solution interface dissolve into the sulfuric solution, the inner ion complexes of the passive layer move to the passive layer/solution interface in order to correlate with the applied potential. The inability of the anions to form oxide implies the continuous formation of metastable ion complexes and dissolution of ions. Since Al easily forms $[Al(SO_4)]^+$ with $(SO_4)^{2-}$, and $Al(OH)SO_4$ with $(SO_4)^{2-}$ and $(OH)^-$, respectively [36], these metastable ion complexes combine with $Cl^-$ and dissolve afterwards. Therefore, pitting easily occurs on the surface of aluminum alloys. Next, the aluminiferous passive layer and non-aluminiferous passive layer are compared. Fig. 10 shows the pitting potential ($E_{pit}$) of the alloys and SS 304 in different solutions. The value of $E_{pit}$ for C-0 is almost independent of chloride concentration. The value of $E_{pit}$ for C-0.25 decreases abruptly for a chloride concentration exceeding 0.50 M. This value is close to that of SS 304. The values of $E_{pit}$, for C-0.25, C-0.50,

and C-1.00, decrease to 0.2-0.5 $V_{SHE}$ at a chloride concentration of 0.25 M (Fig. 10). A higher Al concentration in the alloys implies a lower value of $E_{pit}$. For C-0, deterioration of the passive layer is attributed to the evolution of oxygen. Meanwhile, for C-0.25, C-0.50, and C-1.00, the deterioration of passive layer is attributed to the pitting process. An increasing chloride ion concentration causes the chloride ions to cluster at the defect sites of the passive layer and severely attack the passive layer. Consequently, $E_{pit}$ shifts to a more active region.

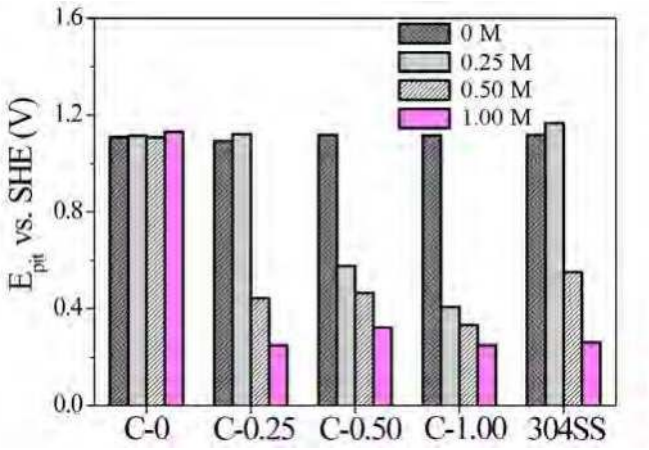


Fig. 10. Histogram of $E_{pit}$ for alloys C-x and SS 304 in solution of different $Cl^-$ ion molarity (M).

### 3.5 Metallographic examination and EDS analysis

Microstructures for not $H_2SO_4$-immersed alloys C-0, C-0.25, C-0.50, and C-1.00 are with single FCC, single FCC, duplex FCC-BCC, and BCC-ordered BCC phases, respectively [6]. Table 6 lists the EDS composition for each phase in different alloys.

| Alloys | Phases and states | Al | Co | Cr | Fe | Ni |
|---|---|---|---|---|---|---|
| C-0 | Overall, not immersed | 0 | 25.93 | 25.73 | 24.21 | 24.13 |
| | Overall, immersed | 0 | 24.45 | 26.39 | 24.83 | 24.32 |
| C-0.25 | Overall, not immersed | 6.16 | 23.27 | 23.58 | 23.59 | 23.40 |
| | Overall, immersed | 6.18 | 23.65 | 24.41 | 23.04 | 22.71 |
| C-0.50 | Overall, not immersed | 11.01 | 22.77 | 22.61 | 21.70 | 21.92 |
| | FCC matrix, not immersed | 8.36 | 24.74 | 23.48 | 22.77 | 20.65 |
| | BCC, not immersed | **13.94** | 21.11 | 20.48 | 20.53 | **23.94** |
| | Overall, immersed | 8.35 | 22.75 | 27.19 | 23.60 | 18.11 |
| | FCC matrix, immersed | 9.96 | 22.57 | 23.16 | 23.59 | 20.72 |
| | Wall-shaped BCC, immersed | **3.82** | 22.50 | **36.33** | 25.58 | **11.77** |
| C-1.00 | Overall, not immersed | 18.88 | 20.55 | 20.63 | 20.01 | 19.93 |
| | Overall, immersed | 12.45 | 19.80 | 29.87 | 23.42 | 14.45 |
| | BCC, immersed | 17.14 | 20.67 | 21.96 | 20.89 | 19.34 |
| | Ordered BCC, immersed | **3.04** | 17.34 | **47.53** | 27.96 | **4.14** |

Table 6. EDS analyses (at %) for alloys C-0, C-0.25, C-0.50, and C-1.00.

Figs. 11(a)-(b) show the microstructure of C-0 before and after 3-d immersion in 0.5 M $H_2SO_4$, respectively. Figs. 11(c)-(d) show the microstructure of C-0.25 before and after 3-d immersion in 0.5 M $H_2SO_4$, respectively. General corrosion occurs for both C-0 and C-0.25, as revealed by EDS analyses (Table 6).

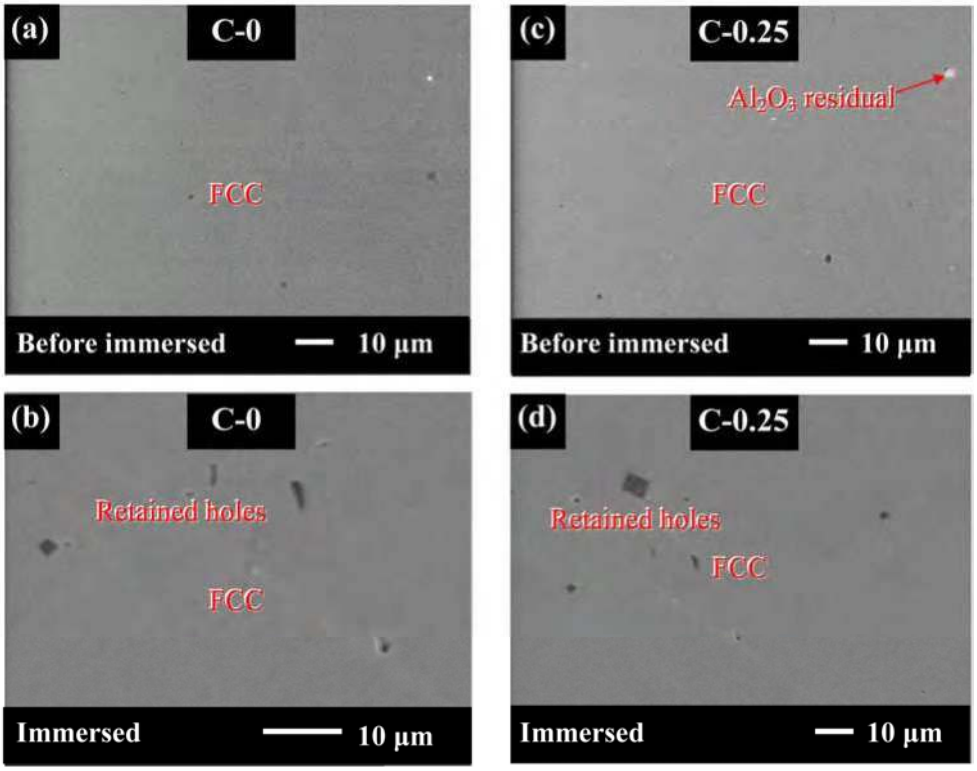


Fig. 11. Metallograph of alloys C-0 ((a) & (b)) and C-0.25 ((c) & (d)). (a) & (c), before; and (b) & (d), after immersion. Retained holes were from cast procedure, and $Al_2O_3$ residuals were from polishing procedure.

Figs. 12(a)-(b) show the microstructure of C-0.50 before and after 3-d immersion in 0.5 M $H_2SO_4$, respectively. According to these figures, after immersion the FCC phase remains smooth while the BCC phase shows a rough morphology. Fig. 12(c) shows a line-scanned area across the FCC and BCC phases for an immersed sample. Fig. 12(d) summarizes the line-scanned results, indicating that the BCC phase of C-0.50 before immersion is rich in Al and Ni. However, after immersion, it is poor in Al and Ni and rich in Cr.

Fig. 13 shows the microstructure and line-scan analysis of C-1.00 before and after immersion. Before immersion, BCC and ordered BCC phases cannot be resolved from the

microstructure. The composition of BCC phase after alloy immersion is close to the overall alloy composition before immersion, indicating that the BCC phase is a corrosion-resistant phase. Moreover, the change in overall composition after immersion is attributed to the selective dissolution of Al and Ni in the ordered BCC phase of this alloy (Table 6).

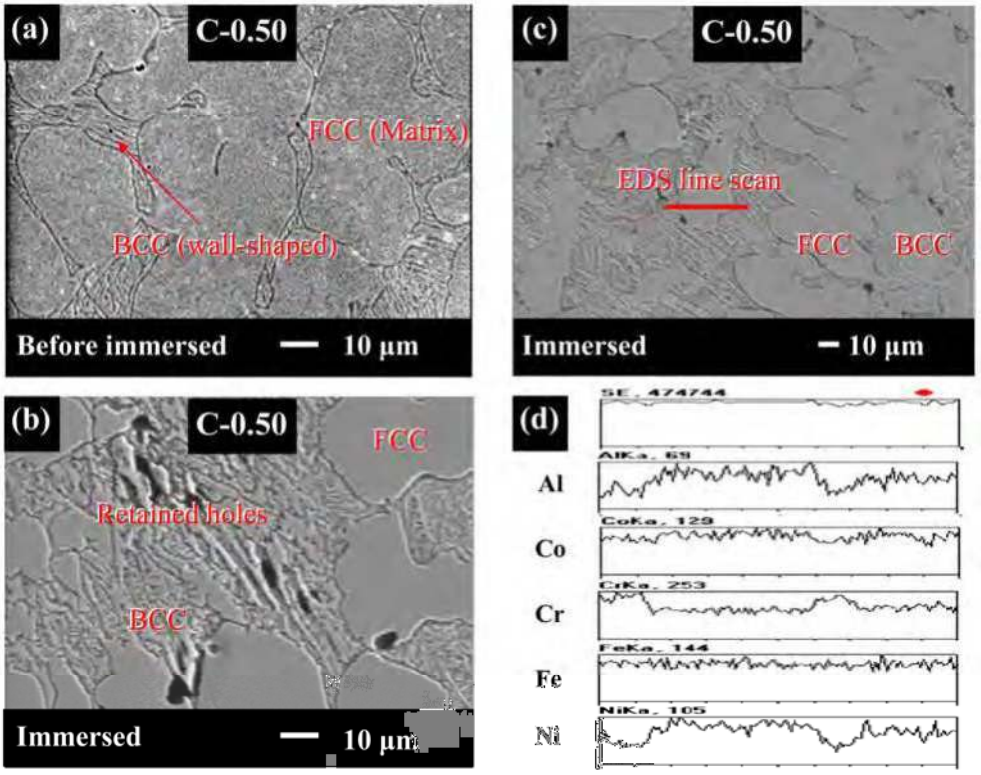


Fig. 12. Metallograph of alloy C-0.50. (a), before; (b) & (c), after immersion; and (d), EDS line-scan results of the location indicated in (c). Retained holes were from cast procedure.

This selective corrosion in Al and Ni-rich phase in C-0.50 and C-1.00, which results in the corrosion attack on Al and Ni, is due to the large bonding in Al and Ni [37]. Alloys containing this bonding readily react with $(OH)^-$ and $(SO_4)^{2-}$ to form Al and Ni complexes and dissolve in a sulfuric solution. Accordingly, after immersion, the remaining compound in the less corrosive-resistant Al and Ni-rich phase is an oxide, rich in Cr, in the residual passive film.

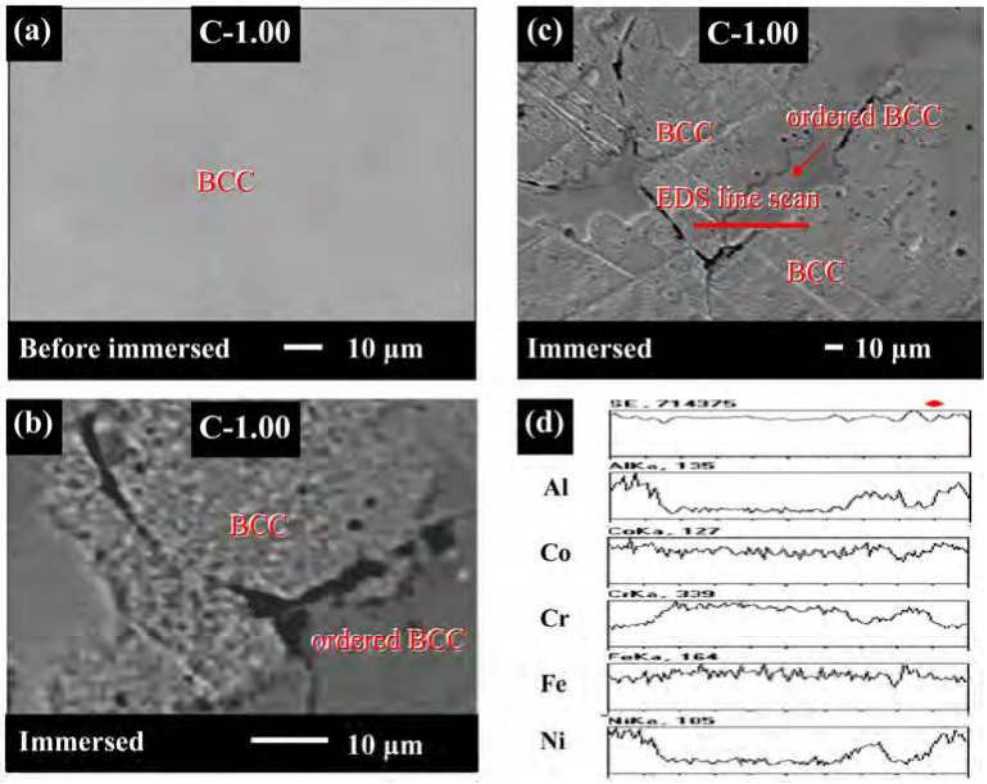


Fig. 13. Metallograph of alloy C-1.00. (a), before; (b) & (c), after immersion; and (d), EDS line-scan results of the location indicated in (c).

### 3.6 Comparison among potentiodynamic polarization, electrochemical impedance spectroscopy, and weight-loss immersion tests

As discussed above, the corrosion current density ($I_{corr}$), the critical current density ($I_{cri}$), and the passive current density ($I_{pass}$) were obtained from potentiodynamic polarization. The capacitance ($Q_f$) and the resistance ($R_f$) of oxide layer were obtained from electrochemical impedance spectroscopy (EIS) equivalent circuits. And the weight-loss rate ($W_{loss}$) was obtained from weight-loss immersion test. All these data were taken from experiments at ambient temperature (25°C) in 0.5 M $H_2SO_4$.

Figs. 14(a)-(b), whose data were listed in Table 2, show $I_{cri}$ and $I_{pass}$ vs. Al content x plots, respectively. One can easily see that both $I_{cri}$ and $I_{pass}$ increase with x. This implies that the passive corrosion property of $Al_xCoCrFeNi$ decreases with Al content x. Fig. 14(c) shows $W_{loss}$ vs. x plot. Like $I_{cri}$ and $I_{pass}$, $W_{loss}$ also increases with x. Notice that, unlike potentiodynamic polarization, immersion weight-loss test is a natural electrochemical reaction, i.e., without applying any voltage on the test sample. On the other hand, $I_{cri}$ and

$I_{pass}$ locate at the passive region of polarization curve. The same tendency for $I_{cri}$, $I_{pass}$, and $W_{loss}$ here indicates that the spontaneous passivation occurs for $Al_xCoCrFeNi$, i.e., the open circuit potential (OCP) is readily in the passive region of polarization curve. The above phenomenon can be attributed to the spontaneous passivation of pure Al in $H_2SO_4$ [24]. EIS equivalent circuits reveal that the passive layers of $Al_xCoCrFeNi$ consist of an oxide layer and an adsorption layer mentioned in Section 3.3. Here, only parameters associated with the oxide layer, i.e., $Q_f$ and $R_f$, are discussed. The oxide layer thickness is evaluated by using the Helmholtz model mentioned above and denoted by d, as $d = \varepsilon\varepsilon_0 S/Q_f$, where $\varepsilon_0$ denotes the permittivity of free space (8.85 x $10^{-14}$ F/cm), ε denotes the dielectric constant of the medium, and S denotes the surface area of the electrode. Assuming that ε and S for oxide layers of alloys are the same allows us to compare relative values of d for all samples by $1/Q_f$. Figs. 14(d)-(e), whose data were listed in Table 5, show the $Q_f$ and $R_f$ vs. x plot, respectively. Both $Q_f$ and $R_f$ decreases with x. This represents that d increases with Al content x, and a thicker oxide layer implies a smaller value of impedance. Therefore, one can explain this phenomenon by considering both the thickness and the density of oxide layer. Related study reported Al oxide easily forms a porous structure [25]. Hence, it is easily understood that in addition to causing a thicker oxide layer, Al promotes the dispersive and porous oxide layer. In summary, Al has a negative effect to the passive parameters, including $I_{cri}$, $I_{pass}$, $W_{loss}$, and $R_f$, for $Al_xCoCrFeNi$ in $H_2SO_4$.

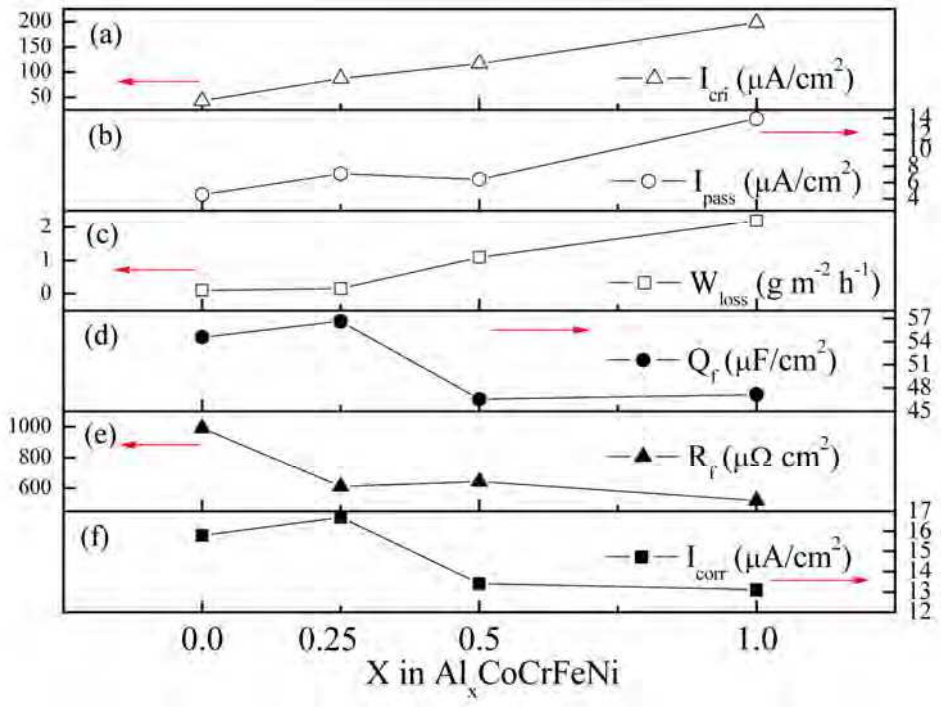


Fig. 14. (a) $I_{cri}$, (b) $I_{pass}$, (c) $W_{loss}$, (d) $Q_f$, (e) $R_f$, and (i) $I_{corr}$ values vs. Al content x plots.

Interestingly, Al makes a different effect on general corrosion. Fig. 14(f) shows $I_{corr}$ vs. x plot. One can see that $I_{corr}$ decreases with x. This implies that Al promotes the general corrosion resistance, but degrades the passive one.

### 3.7 AES, XPS, and ICP-AES analyses of oxide layers

Figs. 15(a)-(d) show the AES results for C-0, C-0.25, C-0.50, and C-1.00, respectively. Owing to the slight difference of atomic number, the signals of Fe, Co, and Ni overlap in AES analysis. Hence, one can see the signals of Co are higher than that of Fe or Ni even for the equal-mole nominal chemical composition of Fe, Co, and Ni. What mentioned above, only the longitudinal composition profiles of O are discussed. A negative and a near-zero slopes are revealed in the relative concentration vs. sputter time profiles in Figs. 15(a)-(d).

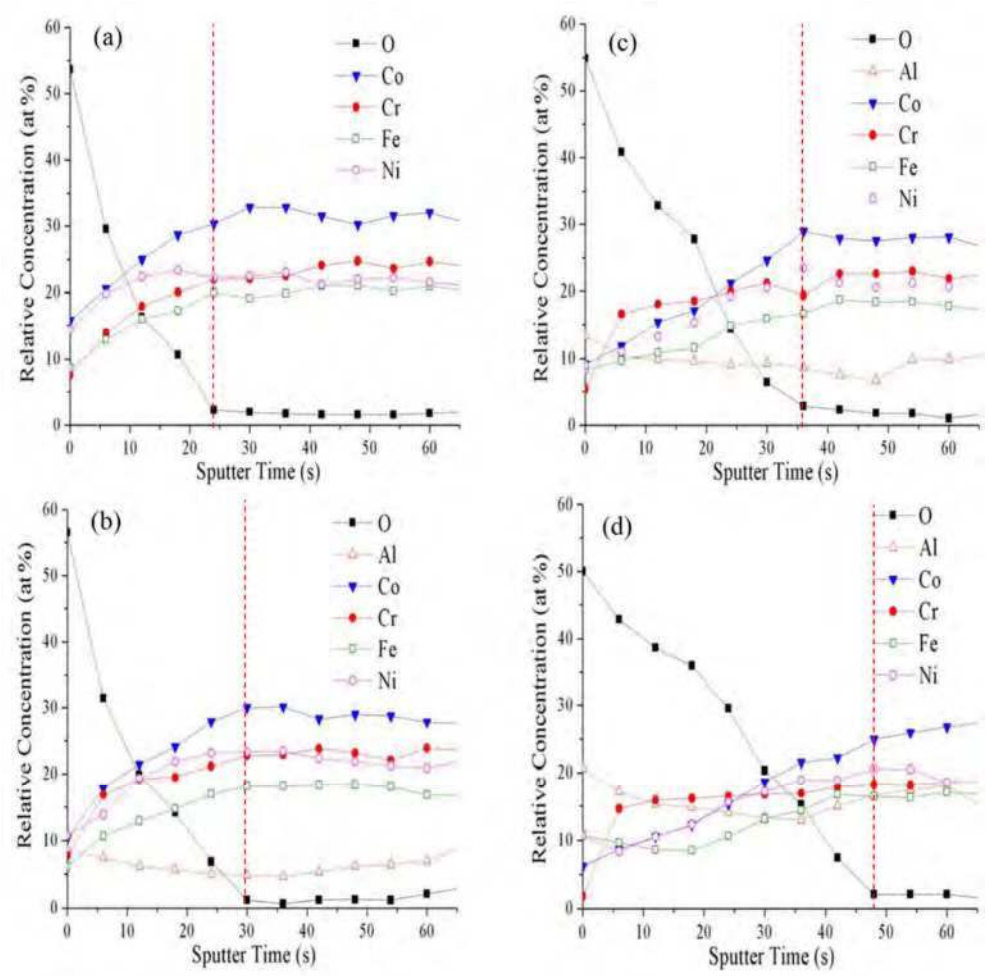


Fig. 15. AES analyses for (a) C-0, (b) C-0.25, (c) C-0.50, and (d) C-1.00.

A value for the identified sputter rate for $SiO_2$ in this AES device is 7.5 nm per min. Because the immersion for the samples is in the same 1-h period of time, the oxide layers of C-0, C-0.25, C-0.50, and C-1.00 can be distinguished from the terminals of the negative slope shown in each of the profiles. Look at the vertical red-dashed line, i.e., the end-terminal of each profile. It represents the interface between the oxide layer and the intrinsic metal. One can see that the thickness of the oxide layer increases with Al content x that is in accordance with the results of EIS.

XPS analyses attempt to investigate the binding energy profile of 2psub<3/2>sub for Al, Co, Cr, Fe, and Ni. Compared to Co, Cr, Fe, and Ni, Al reveals relatively low atomic sensitivity factor [38]. The signals of Al for alloys C-0 to C-0.50 are too small to identify. Hence, only C-1.00 was used for XPS analysis. Figs. 16(a)-(b) show the Al(2psub<3/2>sub) spectra of C-1.00 after the sputter times of 20 and 35 s, respectively. The raw profile revealing two main peaks represents the exhibition of the selective dissolution. The oxides consists of $Al_2O_3$, $Al(OH)_3$, and $Al_{25}Ni_{75}O_x$. Al tends to form oxides in $H_2SO_4$ [24] can explain the formation of $Al_2O_3$ and $Al(OH)_3$. The existence of $Al_{25}Ni_{75}O_x$ results from the relatively negative enthalpy of Al and Ni. Corresponding to the ICP-AES analysis in the next section, Al-Ni selective dissolution undoubtedly exists for C-1.00. Figs. 16(c)-(d) show the Co(2psub<3/2>sub) spectra of C-1.00 after the sputter times of 20 and 35 s, respectively. The binding types of $Co^{2+}$ and $Co^{3+}$ can be seen. Compare Fig. 16(c) with Fig. 16(d), one can see that the peak intensity of $Co_2O_3$ is very small in the deep region of the oxide layer. Figs. 16(e)-(f) show the Cr(2psub<3/2>sub) spectra of C-1.00 after the sputter times of 20 and 35 s, respectively. Three kinds of oxide, including $Cr_2O_3$, $Cr(OH)_3$, and $CrO_3$, exist for Cr [39]. However, $CrO_3$ merely forms at high temperatures. Hence, only $Cr_2O_3$ and $Cr(OH)_3$ are revealed in the profile. One can see that the deep region of oxide layer remains in relatively small amount $Cr_2O_3$. Figs. 16(g)-(h) show the Fe(2psub<3/2>sub) spectra of C-1.00 after the sputter times of 20 and 35 s, respectively. Similar to references [23,40] $Fe_3O_4$ and $Fe_2O_3$ oxides can be found. Figs. 16(i)-(j) show the Ni(2psub<3/2>sub) spectra of C-1.00 after the sputter times of 20 and 35 s, respectively. In resemblance with reference [41], NiO and $Ni(OH)_2$ can be observed. However, a very small amount of $Ni(OH)_2$ appears in our case.

Table 7 lists the results of ICP-AES of immersion solutions for C-x. To trace the ions resulting from the intrinsic metal, one can study the selective dissolution of the alloy elements. Compared with C-0 and C-0.25, C-0.50 and C-1.00 reveal relatively greater Al-Ni selective dissolution. This event is consistent with the results of the XPS analysis.

| Alloys | | Al | Co | Cr | Fe | Ni | Remarks |
|---|---|---|---|---|---|---|---|
| C-0 | alloy | 0 | 25.93 | 25.73 | 24.21 | 24.13 | |
| | solution | 0 | 24.91 | 24.89 | 25.17 | 25.01 | * |
| C-0.25 | alloy | 6.16 | 23.27 | 23.58 | 23.59 | 23.40 | |
| | solution | 7.90 | 23.01 | 23.07 | 23.20 | 22.80 | * |
| C-0.50 | alloy | 11.01 | 22.77 | 22.61 | 21.70 | 21.92 | |
| | solution | 14.92 | 21.90 | 16.51 | 19.96 | 26.70 | ** |
| C-1.00 | alloy | 18.88 | 20.55 | 20.63 | 20.01 | 19.93 | |
| | solution | 31.52 | 20.98 | 4.86 | 14.92 | 27.71 | ** |

*General corrosion, **Selective dissolution in Al and Ni

Table 7. ICP-AES composition (at%) of immersion solution for alloys C-0, C-0.25, C-0.50, and C-1.00.

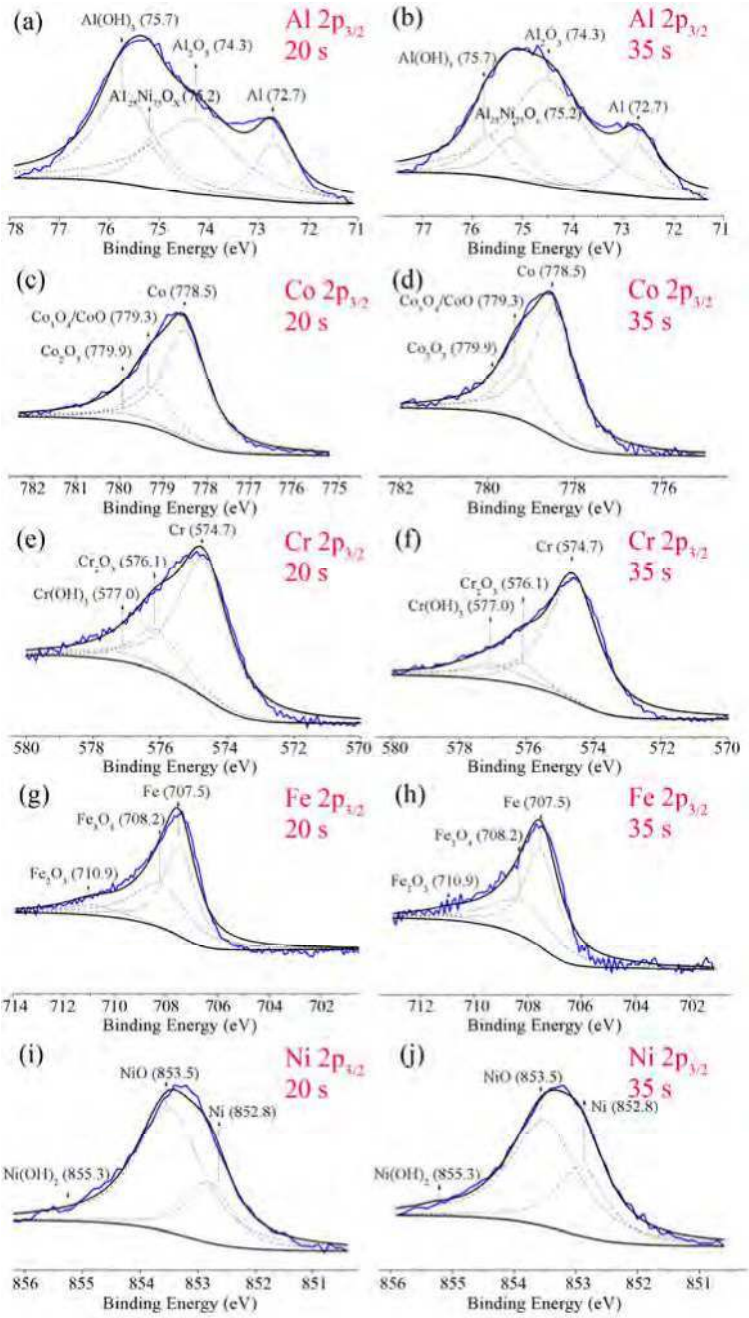


Fig. 16. XPS analyses after pre-sputtering for (a) Al-20 s, (b) Al-35 s, (c) Co-20 s, (d) Co-35 s, (e) Cr-20 s, (f) Cr-35 s, (g) Fe-20 s, (h) Fe-35 s, (i) Ni-20 s, and (j) Ni-35 s.

### 3.8 Corrosion current density ($I_{corr}$) at various temperatures

As mentioned in Section 3.1, $I_{corr}$ decreases with Al content at 25°C. However, this differs from temperatures to temperatures. Fig. 17 shows the $I_{corr}$ values of C-x at various temperatures. One can see that $I_{corr}$ decreases with Al content x at low temperatures (< 27°C), and, conversely, at high temperatures (> 27°C). The EIS results (Section 3.1) indicate that more Al content x makes the oxide layers thicker and more dispersive. At low temperatures, the thicker oxide is the dominator for $I_{corr}$; whereas, at high temperatures, the dispersive oxide dominates. Therefore, this special phenomenon occurs.

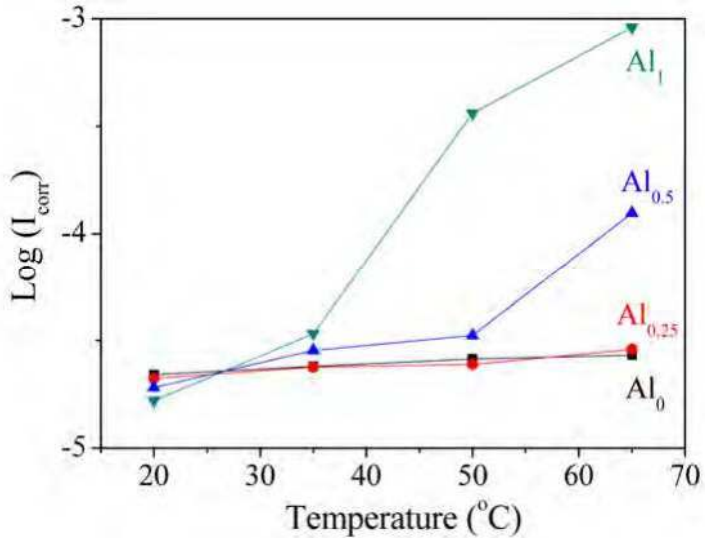


Fig. 17. $I_{corr}$ values for alloys C-x ($Al_x$) at various temperatures.

## 4. Conclusions

Owing to the spontaneous passivation of Al element in $H_2SO_4$, the variation of Al reveals a more apparent effect in a passive region rather than in an active one. Therefore, in contrast with $I_{pass}$, which increases with x, no obvious trends occur for $E_{corr}$ and $I_{corr}$ vs. x variation. In particular, the weight loss experiment indicates that $I_{pass}$ is a proper index to evaluate the weight loss of samples since $Al_xCoCrFeNi$ alloys are found to have passive behaviour in long-term dipping.

EIS results indicate that the passive films of $Al_xCoCrFeNi$ alloys become increasingly thicker and more dispersive with an increasing x. Therefore, $I_{pass}$ increases with x. As x value increases to 1.00, the inductance effect appears in the equivalent circuit for severe dissolution of Al and Ni-rich phase. As for the effect of chloride on the anti-corrosion property, chloride eases the passive layer to form metastable ion complexes and further dissolve into $H_2SO_4$. With an increasing chloride concentration and Al content, the metastable ion complexes easily form, allowing $E_{pit}$ to shift to a more active region. Additionally, the microstructure of both C-0 and C-0.25 is single FCC phase, while those of C-0.50 and C-1.00 are duplex FCC-BCC and complex BCC-ordered BCC phase, respectively.

In C-0.50 and C-1.00, the secondary passivation phenomenon in polarization curve results from selective dissolution of the Al and Ni-rich phase.

Moreover, $I_{corr}$ increases with x at higher temperatures (> 27°C), while $I_{corr}$ decreases with x at lower ones (< 23°C). That more closely examining Arrhenius plots of $I_{corr}$ reveals that both pre-exponential factor A and activation energy $E_a$ increase with Al content. However, A affects $I_{corr}$ more significantly than it does so for $E_a$ at higher temperatures (> 27°C) and, conversely, at lower temperatures (< 23°C).

Al is an inferior factor to the passive corrosive resistance but helpful for the general corrosive resistance for $Al_xCoCrFeNi$ in $H_2SO_4$. The thickness and the density of oxide layers promoted by the addition of Al compete with each other at various temperatures. At ambient temperature, the thick oxide layer dominates $I_{corr}$ value; at temperatures higher than 27°C, the loss oxide layer does. Intuitionally, one may improve the corrosion performance for $Al_xCoCrFeNi$ by adjusting Al content.

## 5. Acknowledgements

The author would like to thank the financial support of this research from the National Science Council of the Republic of China, Taiwan (NSC96-2221-E007-066-MY3). Mr. Yih-Farn Kao is grateful for his help in compilation of this manuscript. This work is mainly from the 2009 master thesis of the Department of Materials Science Engineering of the National Tsing Hua University by Mr. Tsung-Dar Lee, who was guided by the author.

## 6. References

[1] See for example, D.R. Gaskell, Introduction to the Thermodynamics of Materials, 3rd ed., Taylor & Francis, Washington D.C., 1995, p. 204.

[2] K.H. Huang, Multicomponent alloy systems containing equal-mole elements, M.S. thesis, Department of Materials Science and Engineering, NTHU, Taiwan, 1996.

[3] K.T. Lai., Microstructure and properties of multicomponent alloy system with equal-mole elements, M.S. thesis, Department of Materials Science and Engineering, NTHU, Taiwan, 1998.

[4] Y.F. Kao, S.K. Chen, J.H. Sheu, J.T. Lin, W.E. Lin, J.W. Yeh, S.J. Lin, T.H. Liou, C.W. Wang, Hydrogen storage properties of multi-principal-component $CoFeMnTi_xV_yZr_z$ alloys, Int. J. Hydrogen Energy 35 (2010) 9046-9059.

[5] J.W. Yeh, S.K. Chen, S.J. Lin, J.Y. Gan, T.S. Chin, T.T. Shun, C.H. Tsau, S.Y. Chang, Nanostructured high-entropy alloys with multiple principal elements: Novel alloy design concepts and outcomes, Adv. Eng. Mater. 6 (2004) 299-303.

[6] P.K. Huang, J.W. Yeh, T.T. Shun, S.K. Chen, Multi-principal-element alloys with improved oxidation and wear resistance for thermal spray coating, Adv. Eng. Mater. 6 (2004) 74-78.

[7] C.Y. Hsu, J.W. Yeh, S.K. Chen, T.T. Shun, Wear resistance and high-temperature compression strength of FCC $CuCoNiCrAl_{0.5}Fe$ alloy with boron addition, Metall. Mater. Trans. A 35A (2004) 1465-1469.

[8] J. Tong, S.K. Chen, J.W. Yeh, T.T. Shun, C.H. Tsau, S.J. Lin, S.Y. Chang, Mechanical performance of the $Al_xCoCrCuFeNi$ high-entropy alloy system with multiprincipal elements, Metall. Mater. Trans. A 36A (2005) 1263-1271.

[9] J.W. Yeh, S.K. Chen, J.Y. Gan, S.J. Lin, T.S. Chin, T.T. Shun, C.H. Tsau, S.Y. Chang, Formation of simple crystal structures in Cu-Co-Ni-Cr-Al-Fe-Ti-V alloys with multiprincipal metallic elements, Metall. Mater. Trans. A 35A (2004) 2533-2536.

[10] Y.F. Kao, T.J. Chen, S.K. Chen, J.W. Yeh, Microstructure and mechanical property of as-cast, -homogenized, -deformed $Al_xCoCrFeNi$ ($0 \le x \le 2$) high-entropy alloys, J. Alloys & Comp. 488 (2009) 57-64.

[11] H.P. Chou, Y.S. Chang, S.K. Chen, J.W. Yeh, Microstructure, thermophysical and electrical properties in $Al_xCoCrFeNi$ ($0 \le x \le 2$) high-entropy alloys, Mater. Sci. Eng. B 163 (2009) 184-189.

[12] Y.Y. Chen, T. Duval, U.D. Hung, J.W. Yeh, H.C. Shih, Microstructure and electrochemical properties of high entropy alloys—a comparison with type-304 stainless steel, Corros. Sci. 47 (2005) 2257-2279.

[13] Y.Y. Chen, U.T. Hong, H.C. Shih, J.W. Yeh, T. Duval, Electrochemical kinetics of the high entropy alloys in aqueous environments—a comparison with type 304 stainless steel, Corros. Sci. 47 (2005) 2679-2699.

[14] C.P. Lee, C.C. Chang, Y.Y. Chen, J.W. Yeh, H.C. Shih, Effect of the aluminium content of $Al_xCrFe_{1.5}MnNi_{0.5}$ high-entropy alloys on the corrosion behaviour in aqueous environments, Corros. Sci. 50 (2008) 2053-2060.

[15] C.P. Lee, Y.Y. Chen, C.Y. Hsu, J.W. Yeh, H.C. Shih, Enhancing pitting corrosion resistance of $Al_xCrFe_{1.5}MnNi_{0.5}$ high-entropy alloys by anodic treatment in sulfuric acid, Thin Solid Films 517 (2008) 1301-1305.

[16] C. P. Lee, Y. Y. Chen, C. Y. Hsu, J. W. Yeh, and H. C. Shih, The Effect of Boron on the Corrosion Resistance of the High-Entropy Alloys $Al_{0.5}CoCrCuFeNiB_x$, J. Electrochem. Soc., 154 (2007) C424-C430.

[17] Y.F. Kao, T.D. Lee, S.K. Chen, Y.S. Chang, Electrochemical passive properties of $Al_xCoCrFeNi$ (x = 0, 0.25, 0.50, 1.00) alloys in sulfuric acids, Corros. Sci. 52 (2010) 1026-1034.

[18] V. Ashworth, P.J. Boden, Potential-pH diagrams at elevated temperatures, Corros. Sci. 10 (1970) 709-718.

[19] Y.Y. Chen, L.B. Chou, L.H. Wang, J.C. Oung, H.C. Shih, Electrochemical polarization and stress corrosion cracking of alloy 690 in 5-M chloride solutions at 25°C, Corros. 61 (2005) 3-11.

[20] M. Femenia, J. Pan, C. Laygraf, In situ local dissolution of duplex stainless steels in 1 M $H_2SO_4$ + 1 M NaCl by electrochemical scanning tunneling microscopy, J. Electrochem. Soc. 149 (2002) B187-B197.

[21] I.H. Lo, W.T. Tsai, Effect of selective dissolution on fatigue crack initiation in 2205 duplex stainless steel, Corros. Sci. 49 (2007) 1847-1861.

[22] F. D. Bogar, M. H. Peterson, A comparison of actual and estimated long-term corrosion rate of mild steel in seawater, Laboratory Corrosion Test and Standards, ASTM STP 866 (1985) 197-206.

[23] P. Marcus, Corrosion Mechanisms in Theory and Practice, 2nd ed., Marcel Dekker, New York, 2002.

[24] V. Shankar Rao, V.S. Raja, Anodic polarization and surface composition of Fe-16Al-0.14C alloy in 0.25 M sulfuric acid, Corros. 59 (2003) 575-583.
[25] L. Young, Anodic Oxide Films, 1st ed., Academic Press, London, 1961.
[26] G.K. Gomma, Corrosion of low-carbon steel in sulphuric acid solution in presence of pyrazole-halides mixture, Mater. Chem. & Phys. 55 (1998) 241-246.
[27] C.F. Zinola, A.M. Castro Luna, The inhibition of Ni corrosion in $H_2SO_4$ solutions containing simple non-saturated substances, Corro. Sci. 37 (1995) 1919-1929.
[28] M.R.F. Hurtado, P.T.A. Sumodjo, A.V. Benedetti, Electrochemical studies with a Cu-5 wt.% Ni alloy in 0.5 M $H_2SO_4$, Electrochimica Acta 48 (2003) 2791-2798.
[29] F.M Reis, H.G. de Melo, I. Costa, EIS investigation on Al 5052 alloy surface preparation for self-assembling monolayer, Electrochimica Acta 51 (2006) 1780-1788.
[30] T.M. Yue, L.J. Yan, C.P. Chan, C.F. Dong, H.C. Man, G.K.H. Pang, Excimer laser surface treatment of aluminum alloy AA7075 to improve corrosion resistance, Surface and Coating Technology 179 (2004) 158-164.
[31] I. Epelboin, C. Gabrielle, M. Keddam, H. Takenouti, Achievements and tasks of electrochemical engineering, Electrochimica Acta 22 (1975) 913-920.
[32] M. Metikoš-Huković, R. Babić, S. Brinić, EIS-in situ characterization of anodic films on antimony and lead-antimony alloys, J. Power Sources 157 (2006) 563-570.
[33] A.R. Trueman, Determining the probability of stable pit initiation on aluminium alloys using potentiostatic electrochemical measurements, Corros. Sci. 47 (2005) 2240-2256.
[34] Y.M. Tang, Y. Zuo, X.H. Zhao, The metastable pitting behaviours of mild steel in bicarbonate and nitrite solutions containing $Cl^-$, Corros. Sci. 50 (2008) 989-994.
[35] R.T. Foley, T.H. Nguyen, The chemical nature of aluminum corrosion, J. Electrochem. Soc. 129 (1982) 464-467.
[36] S. Van Gils, C.A. Melendres, H. Terryn, E. Stijns, Use of in-situ spectroscopic ellipsometry to study aluminium/oxide surface modifications in chloride and sulfuric solutions, Thin Solid Films 455 (2004) 742-746.
[37] H. Nakazawa, H. Sato, Bacterial leaching of cobalt-rich ferromanganese crusts, International Journal of Mineral Processing 43 (1995) 255-265.
[38] C.D. Wagner, W.M. Riggs, L.E. Davis, J.F. Moulder, G.E. Muilenberg, Handbook of X-Ray Photoelectron Spectroscopy, 1st ed., Perkin-Elmer Corporation, Minnesota, 1979.
[39] A.A. Hermas, M. Nakayama, K. Ogura, Formation of stable passive film on stainless steel by electrochemical deposition of polypyrrole, Electrochimica Acta 50 (2005) 3640-3647.
[40] K. Varga, P. Baradlai, W.O. Barnard, G. Myburg, P. Halmos, J.H. Potgieter, Comparative study of surface properties of austenitic stainless steels in sulfuric and hydrochloric acid solutions, Electrochimica Acta 42 (1997) 25-35.
[41] R. Wang, An AFM and XPS study of corrosion caused by micro-liquid of dilute sulfuric acid on stainless steel, Appl. Surf. Sci. 227 (2004) 399-409.


**Corrosion Resistance**

Edited by Dr Shih

ISBN 978-953-51-0467-4
Hard cover, 472 pages
**Publisher** InTech
**Published online** 30, March, 2012
**Published in print edition** March, 2012

The book has covered the state-of-the-art technologies, development, and research progress of corrosion studies in a wide range of research and application fields. The authors have contributed their chapters on corrosion characterization and corrosion resistance. The applications of corrosion resistance materials will also bring great values to reader's work at different fields. In addition to traditional corrosion study, the book also contains chapters dealing with energy, fuel cell, daily life materials, corrosion study in green materials, and in semiconductor industry.

**How to reference**

In order to correctly reference this scholarly work, feel free to copy and paste the following:

Swe-Kai Chen (2012). Electrochemical Passive Properties of AlxCoCrFeNi (x = 0, 0.25, 0.50, 1.00) High-Entropy Alloys in Sulfuric Acids, Corrosion Resistance, Dr Shih (Ed.), ISBN: 978-953-51-0467-4, InTech, Available from: http://www.intechopen.com/books/corrosion-resistance/electrochemical-passive-properties-of-alxcocrfeni-x-0-0-25-0-50-1-00-high-entropy-alloys-in-sulfuric

INTECH
open science | open minds

**InTech Europe**
University Campus STeP Ri
Slavka Krautzeka 83/A
51000 Rijeka, Croatia
Phone: +385 (51) 770 447
Fax: +385 (51) 686 166
www.intechopen.com

**InTech China**
Unit 405, Office Block, Hotel Equatorial Shanghai
No.65, Yan An Road (West), Shanghai, 200040, China
中国上海市延安西路65号上海国际贵都大饭店办公楼405单元
Phone: +86-21-62489820
Fax: +86-21-62489821